Supporting Information for 'The Thermal Structure and Composition of Jupiter's Great Red Spot from JWST/MIRI'

Jake Harkett[1], Leigh N. Fletcher[1], Oliver R.T. King[1], Michael T. Roman[1], Henrik Melin[1], Heidi B. Hammel[2], Ricardo Hueso[3], Agustín Sánchez-Lavega[3], Michael H. Wong[4], Stefanie N. Milam[5], Glenn S. Orton[6], Katherine de Kleer[7], Patrick G.J. Irwin[8], Imke de Pater[9], Thierry Fouchet[10], Pablo Rodríguez-Ovalle[10], Patrick M. Fry[11], Mark R. Showalter[12]

[1]School of Physics and Astronomy, University of Leicester, University Road, Leicester LE1 7RH, UK
[2]Association of Universities for Research in Astronomy, Suite 1475, 1331 Pennsylvania Avenue NW, Washington DC 20004, USA
[3]Escuela de Ingeniería de Bilbao, Universidad del País Vasco, UPV/EHU, Bilbao, Spain
[4]Center for Integrative Planetary Science, University of California, Berkeley, CA 94720, USA
[5]Astrochemistry Laboratory Code 691, NASA Goddard Space Flight Center, 8800 Greenbelt Road, Greenbelt MD 20771, USA
[6]Jet Propulsion Laboratory, California Institute of Technology, Pasadena, CA 91109, USA
[7]Division of Geological and Planetary Sciences, California Institute of Technology, Pasadena, CA 91125, USA
[8]Department of Physics, University of Oxford, Parks Rd, Oxford, OX1 3PU, UK
[9]Department of Astronomy, University of California, Berkeley, California 94720, USA
[10]LESIA, Observatoire de Paris, Université PSL, CNRS, Sorbonne Université, Université Paris-Cité, Meudon, France
[11]Space Science and Engineering Center, University of Wisconsin, 1225 west Dayton Street, Madison, WI, 53706, USA
[12]SETI Institute, 189 Bernardo Ave., Mountain View, CA 94043, USA

Contents of this file

1. Text S1 to S13

Introduction

This supplemental file contains figures that support the main text, providing additional context.

Fig. S1 - S3 discusses our methodology for deriving the flat-field solution used in this study. Fig. S4 displays 2D maps of the spectral uncertainties for a range of wavelengths containing contribution from both the troposphere and the stratosphere. Fig. S5 highlights the issues we experienced fitting the CH_4 Q-branch at 7.66 µm. Fig. S6 and S7 display 3D graphics of the retrieved tropospheric and stratospheric temperature structure within the MIRI FOV. An image taken by Hubble was used for visible-light context of the cloud tops in July. In August, visible amateur data is displayed that was observed on 2022-08-15 (Miyazaki, 2024). Fig. S8 compares the differences in temperature between the July and August epochs. Fig. S9 displays 2D maps of the temperature retrieval uncertainty (1σ). Fig. S10 displays the correlation (or lack thereof) between NH_3 FSH and Saturation Vapor Pressure (SVP) derived from the retrieved temperature structure and between PH_3 FSH and retrieved aerosol opacity. The NH_3 shows little difference in the correlation between SVP and NH_3 FSH between the outside and inside of the GRS vortex. The PH_3 does display a good correlation, but only inside the GRS vortex. This is consistent with the theory of the PH_3 molecules inside the GRS being shielded by the excess aerosol opacity from the UV light that would normally photolyse and remove this molecule as outlined in the main text.

Corresponding author: Jake Harkett, `jh852@leicester.ac.uk`

Fig. S11 displays the calculated 2D Jovian gravity field used to derive the thermal winds in the main text. This was dependent on the planetocentric latitude (ϕ_c) and the altitude above the 1 bar pressure level (z) and is given by:

$$g(\phi_c, z) = \frac{GM_J}{(R+z)^2} \tag{1}$$

where G is the gravitational constant, M_J is the mass of Jupiter, taken as 1.898×10^{27} kg and:

$$R = \frac{R_{eq}}{\sqrt{(\cos\phi_c)^2 + (\frac{1}{1-e})^2(\sin\phi_c)^2}} \tag{2}$$

where R_{eq} is the equatorial radius of Jupiter, taken as 71492 km and e is the jovian ellipticity, taken as 0.065.

Finally, Fig. S12 and S13 display 2D maps of the thermal windshear uncertainties, thermal velocity uncertainty and buoyancy frequency uncertainty.

References

Fletcher, L. N., King, O. R. T., Harkett, J., Hammel, H. B., Roman, M. T., Melin, H., . . . Tiscareno, M. S. (2023, September). Saturn's Atmosphere in Northern Summer Revealed by JWST/MIRI. *Journal of Geophysical Research (Planets)*, *128*(9), e2023JE007924. doi: 10.1029/2023JE007924

Greenfield, P., & Miller, T. (2016, July). The Calibration Reference Data System. *Astronomy and Computing*, *16*, 41-53. doi: 10.1016/j.ascom.2016.04.001

Irwin, P. G. J., Teanby, N. A., de Kok, R., Fletcher, L. N., Howett, C. J. A., Tsang, C. C. C., . . . Parrish, P. D. (2008, April). The NEMESIS planetary atmosphere radiative transfer and retrieval tool. *JQSRT*, *109*, 1136-1150. doi: 10.1016/j.jqsrt.2007.11.006

King, O. R. T., Fletcher, L. N., Harkett, J., Roman, M. T., & Melin, H. (2023, October). Custom JWST NIRSpec/IFU and MIRI/MRS Data Reduction Pipelines for Solar System Targets. *Research Notes of the American Astronomical Society*, *7*(10), 223. doi: 10.3847/2515-5172/ad045f

Law, D. R., E. Morrison, J., Argyriou, I., Patapis, P., Álvarez-Márquez, J., Labiano, A., & Vandenbussche, B. (2023, August). A 3D Drizzle Algorithm for JWST and Practical Application to the MIRI Medium Resolution Spectrometer. *AJ*, *166*(2), 45. doi: 10.3847/1538-3881/acdddc

Leovy, C. B., Friedson, A. J., & Orton, G. S. (1991, December). The quasiquadrennial oscillation of Jupiter's equatorial stratosphere. *Nature*, *354*(6352), 380-382. doi: 10.1038/354380a0

Miyazaki, I. (2024). *Jupiter: Images from Okinawa Island [Data].* Retrieved from `http://www.ii-okinawa.ne.jp/people/miyazaki/planet/`

Orton, G. S., Friedson, A. J., Caldwell, J., Hammel, H. B., Baines, K. H., Bergstralh, J. T., . . . Shure, M. (1991, April). Thermal maps of Jupiter - Spatial organization and time dependence of stratospheric temperatures, 1980 to 1990. *Science*, *252*(5005), 537-542. doi: 10.1126/science.252.5005.537

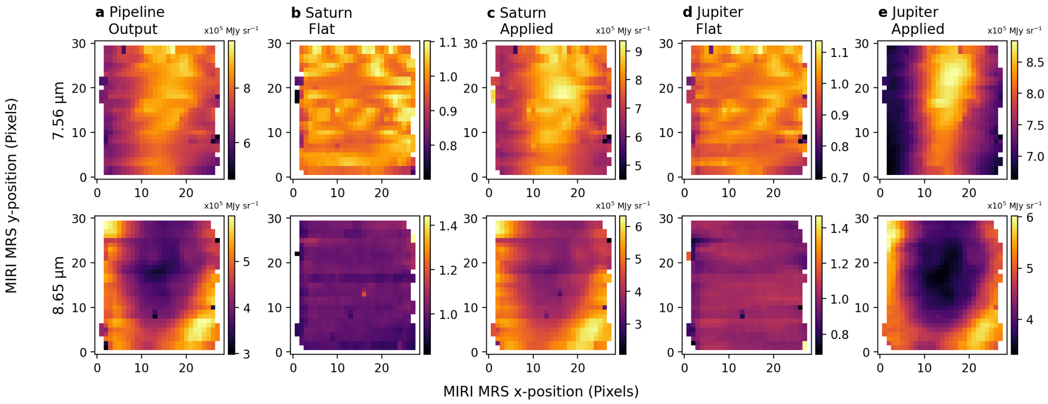

Figure S1: (a) Output from stage 3 of the JWST calibration pipeline (Greenfield & Miller, 2016) for 7.56 µm, containing contribution from the jovian stratosphere and 8.65 µm, displaying contribution from the troposphere. Dither 1 of the Central tile of the July Epoch is shown here. The GRS is visible in the latter wavelength as an oval of low surface-brightness. Flat-fielding effects such as horizontal stripes and artefacts are visible for both wavelengths. (b) Flat field frames derived using data from Saturn as part of observation GTO 1247 (Fletcher et al., 2023; King et al., 2023). A flat-field was derived for each observation in this sequence using the 4 dither positions for each tile and the average of these is presented here. (c) Applying this derived Saturn flat did little to resolve the problems seen in the Jupiter data. (d) Flat-fields derived using the Jupiter GTO 1246 data, again taking the average of all the flat-fields derived from each of the observations. (e) Applying this mean Jupiter flat to the Jupiter data improved the data quality, but did not fully resolve the flat-fielding problems.

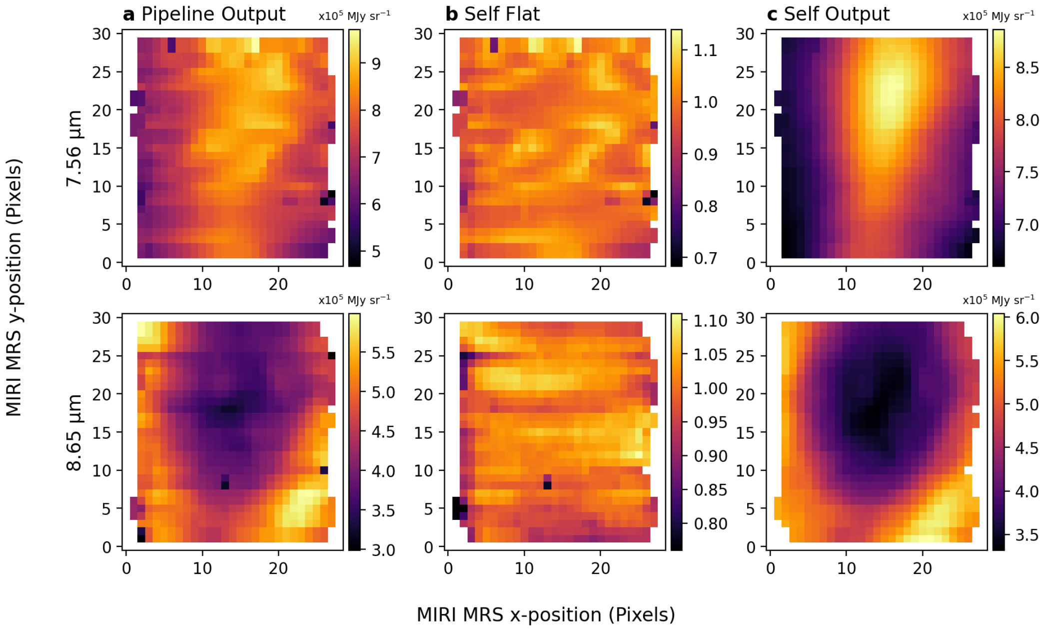

Figure S2: The July/Centre/dither 1 data is again shown here. (a) Deriving a mean flat-field using the Jupiter GTO 1246 data following the approach of (Fletcher et al., 2023; King et al., 2023) in Fig. S1 did not fully remove the stripes and artefacts observed in the stage 3 pipeline output. (b) New flat-fields were therefore derived using the 4 dither positions for each tile. This generated flat-fields that were unique to each tile. Note that there was still sufficient spatial separation between the dither positions to avoid atmospheric structure appearing in these flats. (c) Applying these new flat-field solutions to the data resulted in considerable improvement to the data quality, with previously obscured atmospheric structure becoming visible.

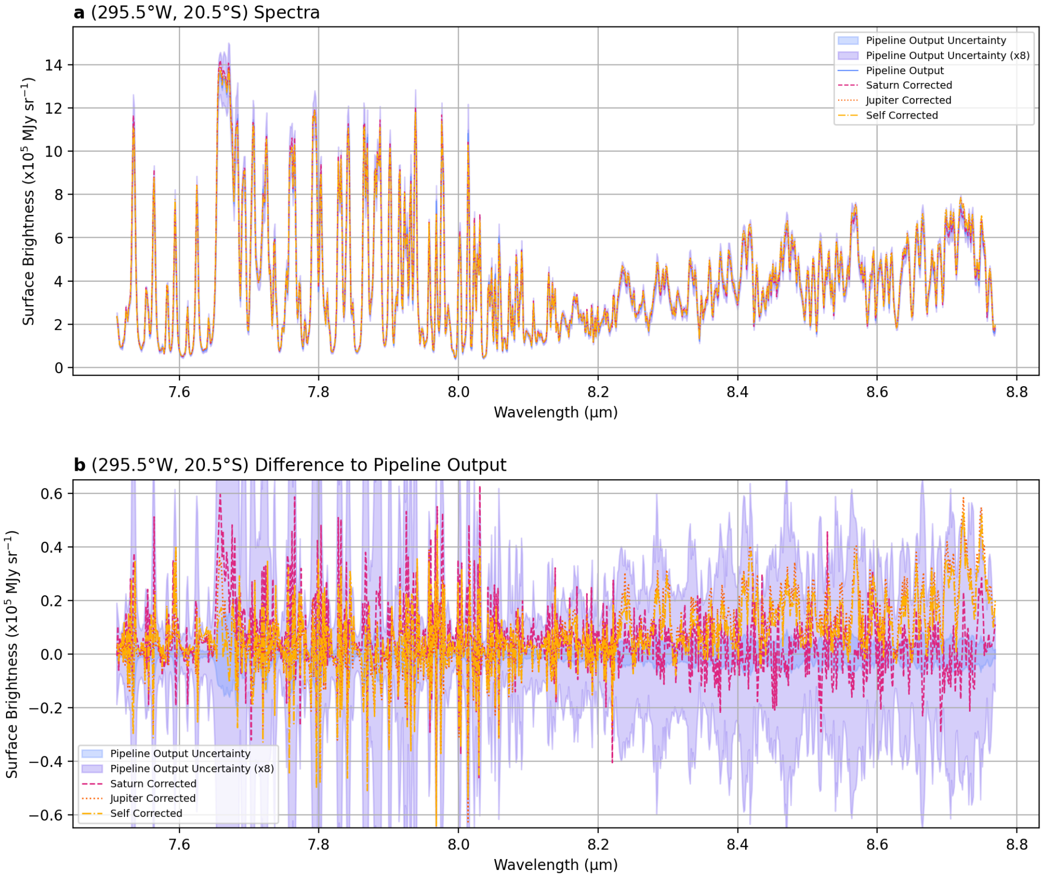

Figure S3: (a) Spectra obtained from (295.5°W, 20.5°S) corresponding to the approximate centre of the FOV in Fig. S1 and S2 for the stage 3 pipeline output and each version of the flat-field solution. The pipeline output uncertainty, although indicated on the plot is too small to be seen here due to a known issue where the pipeline currently underestimates spectral uncertainties by a factor of 10 (Law et al., 2023). Multiplying this by factors of 4-8 (8 shown here) enabled us to achieve better fitting in the retrieval process. (b) Difference of each flat-field corrected spectrum to the pipeline output. The uncertainties (normal and multiplied by 8) in the pipeline output are indicated by the shaded regions. Mean standard deviation across the wavelength range at this position for the Saturn Corrected, Jupiter corrected and Self-Corrected data was; 1.17, 1.84 and 1.65 respectively. However, accounting for the underestimated pipeline uncertainties, the difference in surface brightness between the flat-field corrected and the pipeline output data is typically a factor of 0.2 - 0.5 smaller than the spectral uncertainties and was therefore ignored.

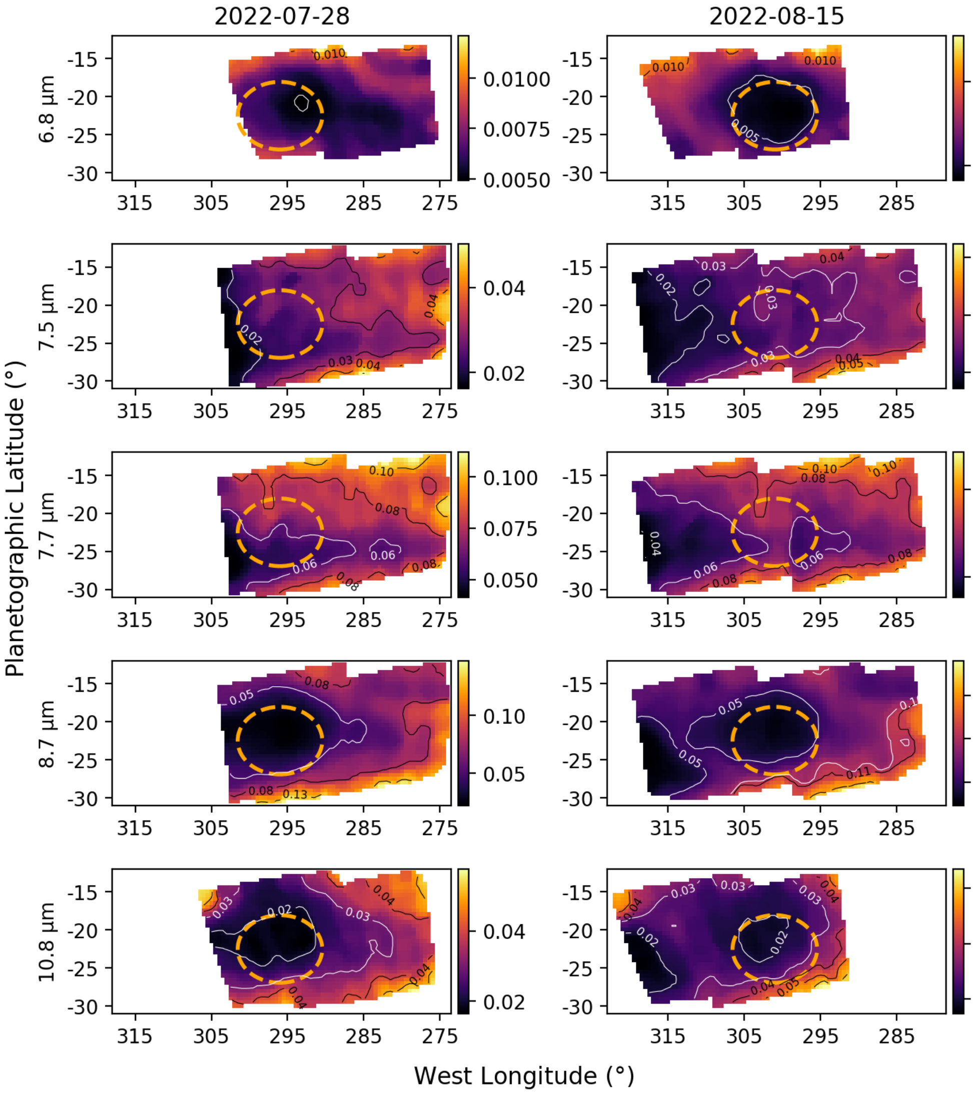

Figure S4: 2D maps of the spectral radiance (µW cm^2 sr^{-1} µm^{-1}) uncertainties for; 6.8 µm (probing 800 mbar), 7.5 µm (10 mbar), 7.7 µm (1 mbar), 8.7 µm (1000 mbar) and 10.8 µm (400 mbar). The positions of the peak Hubble wind velocities are indicated by the dashed orange circle. The first column displays the July epoch uncertainties, the GRS is centred on (296.0°W, 22.5°S). The second column displays the August data, the GRS here is centred on (301.0°W, 22.5°S).

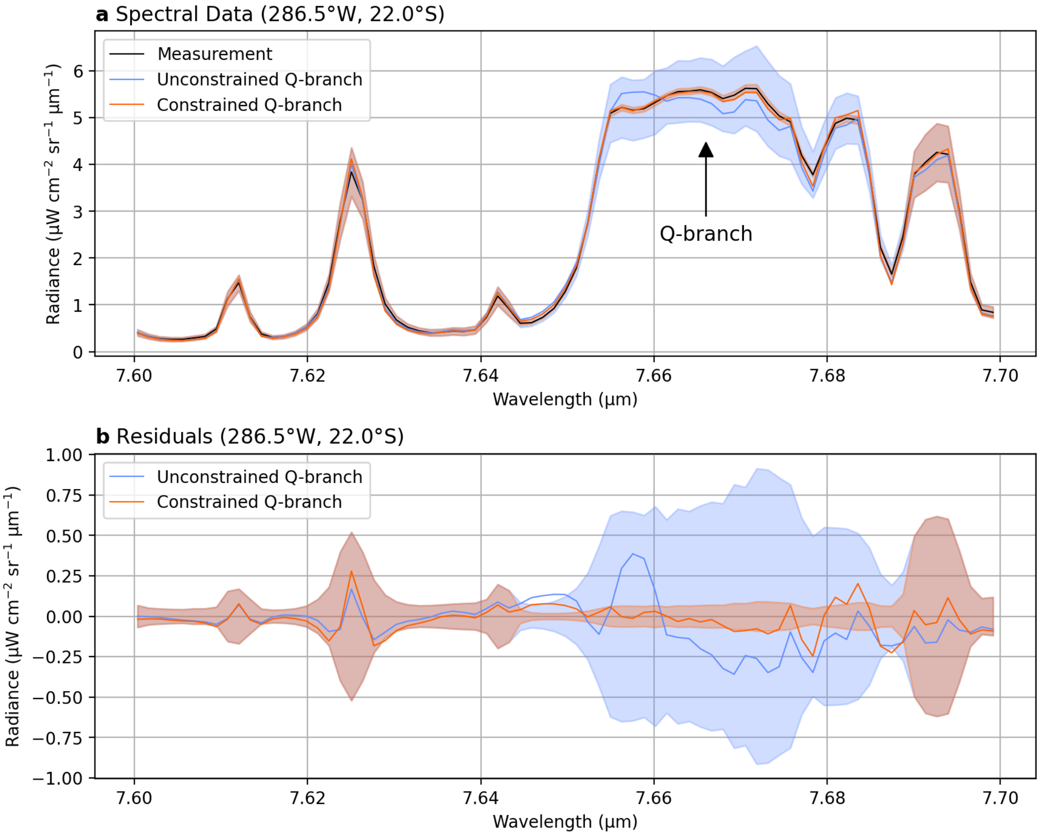

Figure S5: (a) Stage 2 spectral fits to (286.5°W, 22.0°S). The uncertainties obtained from the JWST calibration pipeline and multiplied by 8 to account for the known issue of the pipeline underestimating uncertainties (Law et al., 2023) resulted in the CH_4 Q-branch being unconstrained, resulting in deviation between the data and model. Dividing these uncertainties by a factor of 10.0 in the 7.656 μm - 7.678 μm range resulted in smaller residuals in this region that were comparable in magnitude to the surrounding (well-fitted) wavelengths (b). The CH_4 Q-branch contains contribution from the highest altitudes within this wavelength range, sensing temperatures at the 1 mbar level and above. Constraining the spectral uncertainties in this Q-branch improved our ability to probe temperatures in the jovian stratosphere.

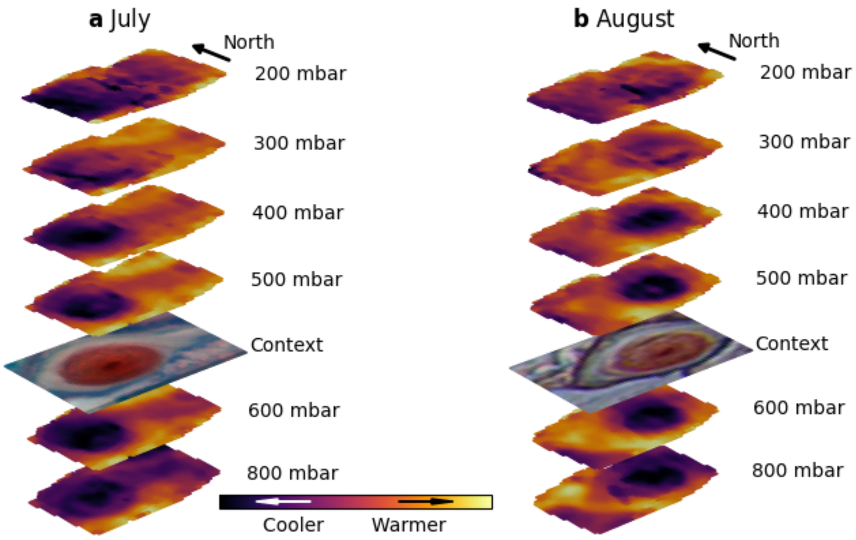

Figure S6: 3D graphic displaying the tropospheric temperatures within the MIRI FOV for July (a) and August (b). Stage 1 retrieval data is visualised here. Visual context images from Hubble and Amateur ground-based observations are provided for July and August respectively. The cold temperature anomaly dominates this FOV at the full range of altitudes. However, the well-contrasted vortex structure begins to break down at higher altitudes approaching the tropopause.

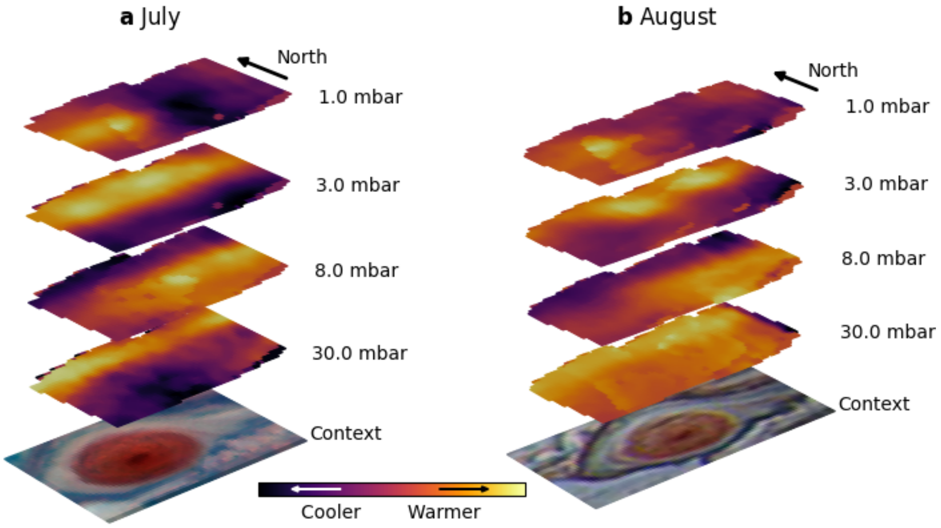

Figure S7: 3D graphic displaying the temperature structure of the stratosphere above the GRS. Visual context observations provided by Hubble in July (a) and ground-based observers in August (b) are also displayed. Below 3 mbar, the temperature structure is dominated by the Jovian QQO (Orton et al., 1991; Leovy et al., 1991). Little east-west variation is seen at these lower altitudes. At 3 mbar, the two hot-spots residing either side of the GRS become visible.

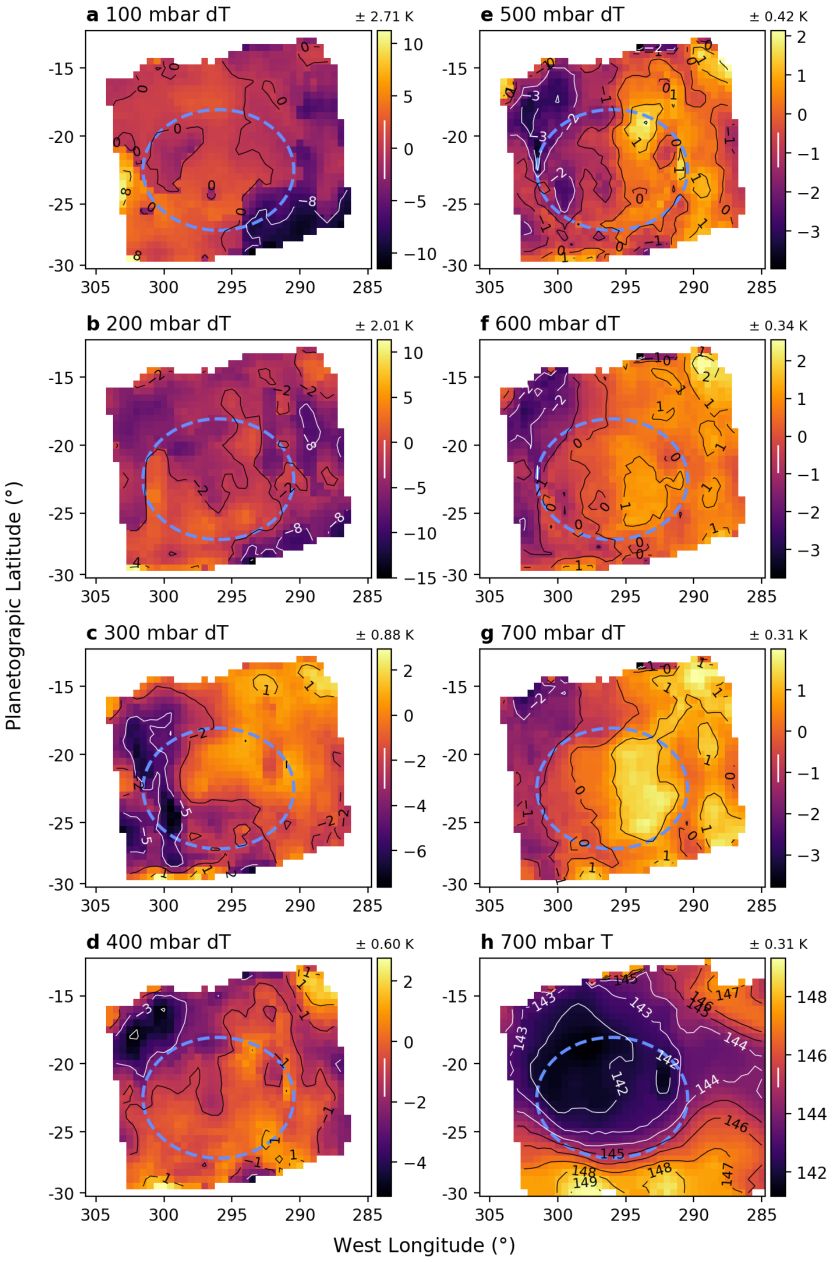

Figure S8: (a) to (g) temperature difference (dT) between the two MIRI epochs (July - August) for a range of tropospheric altitudes. Note only the central tile is visible here since the western tile for July and the eastern tile for August are missing. (h) Context temperature (T) map for the July epoch, centred on the 700 mbar pressure level and at the same scale as the temperature difference plots. For all plots, the ring of peak wind velocities is denoted by the blue dashed circle. The 1σ temperature uncertainties for each altitude are denoted by the vertical line in the colour bar, while the contour lines are spaced by 3σ to aid interpretation. No large-scale changes to the structure of the GRS or the surroundings can be seen in these plots. Although the region north-west of the GRS is 3 ± 1 K cooler at this altitude range, this is most likely to be a retrieval artefact, potentially generated by the degeneracies observed between the 4 parameters retrieved in this study.

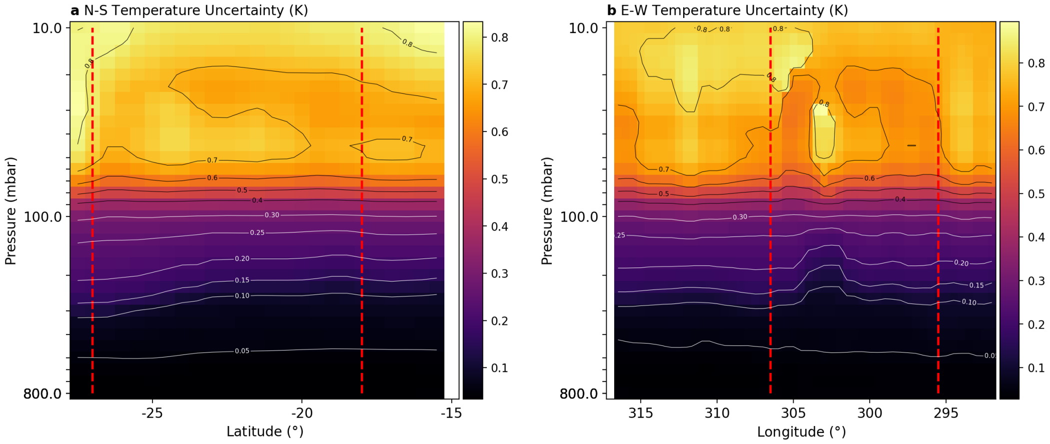

Figure S9: (a) 2D north-south temperature uncertainty map for the August epoch passing through the centre of the GRS at 301.0°W. (b) Corresponding derived temperature uncertainty for the east-west direction, passing through 22.5°S. The positions of the peak Hubble velocity fields around the edge of the GRS are denoted by vertical dashed lines.

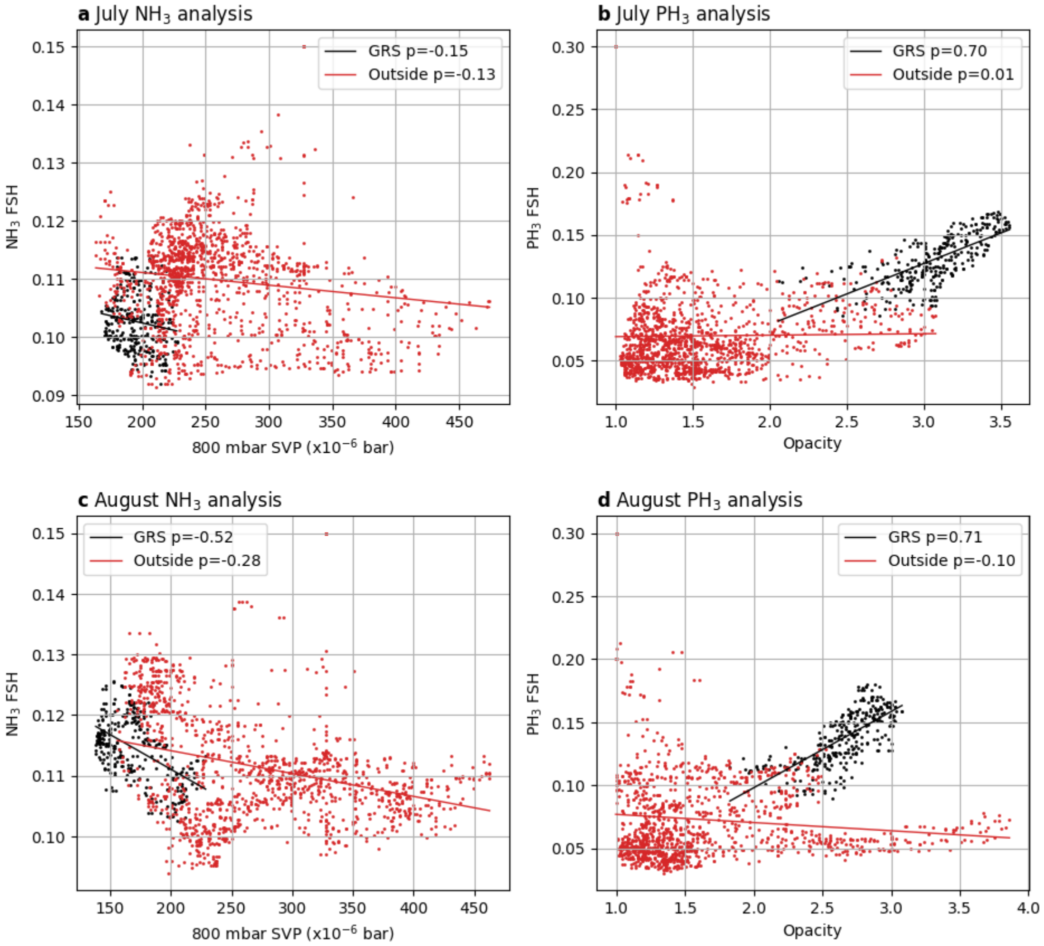

Figure S10: Analysis of the correlation between NH_3 FSH and 800 mbar NH_3 Saturation Vapor Pressure (SVP), derived using SVP $= e^{A+\frac{B}{T}+CT+DT^2}$. Where $A = 23.224$, $B =$ -4245.8, $C =$ -2.2775 $\times$ 10^{-2} and $D = 0.0$ (Irwin et al., 2008). The results are displayed for July (a) and August (c). No discernible differences were found between inside and outside the GRS. (b) and (d) display the correlation between PH_3 FSH and integrated aerosol opacity for July and August respectively. In both epochs, these two parameters display a strong correlation inside the GRS and little correlation outside. This is consistent with the aerosol opacity shielding the PH_3 from the UV light that would normally photolyse and remove this molecule, allowing it to accumulate above the GRS.

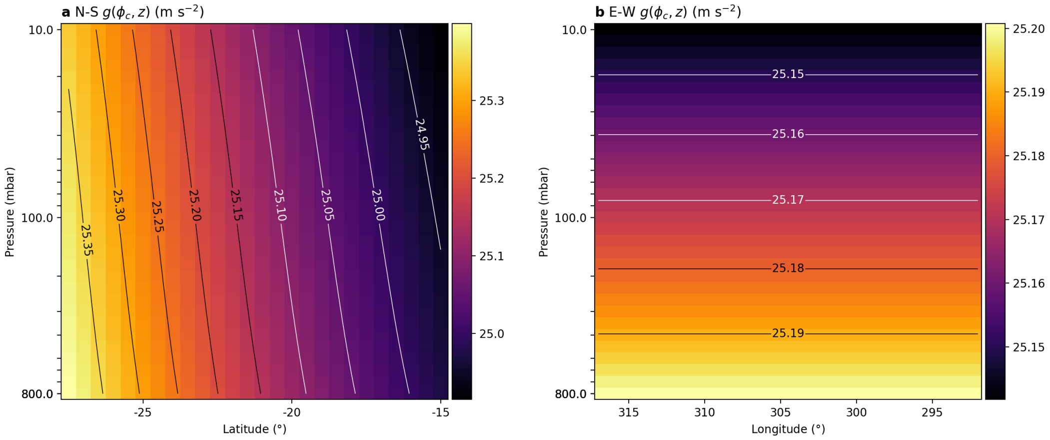

Figure S11: Estimates of the 2D Jovian gravity field given by Equation 1. Note in the main text and indeed in all other supplemental figures, planetographic latitude is used. These were derived for the thermal wind calculations in both the (a) north-south direction centred on 301.0°W and (b) the east-west direction centred on 22.5°S. Note that the effect of ϕ_c on g in the zonal direction far outweighs the minor change in gravitational acceleration with z.

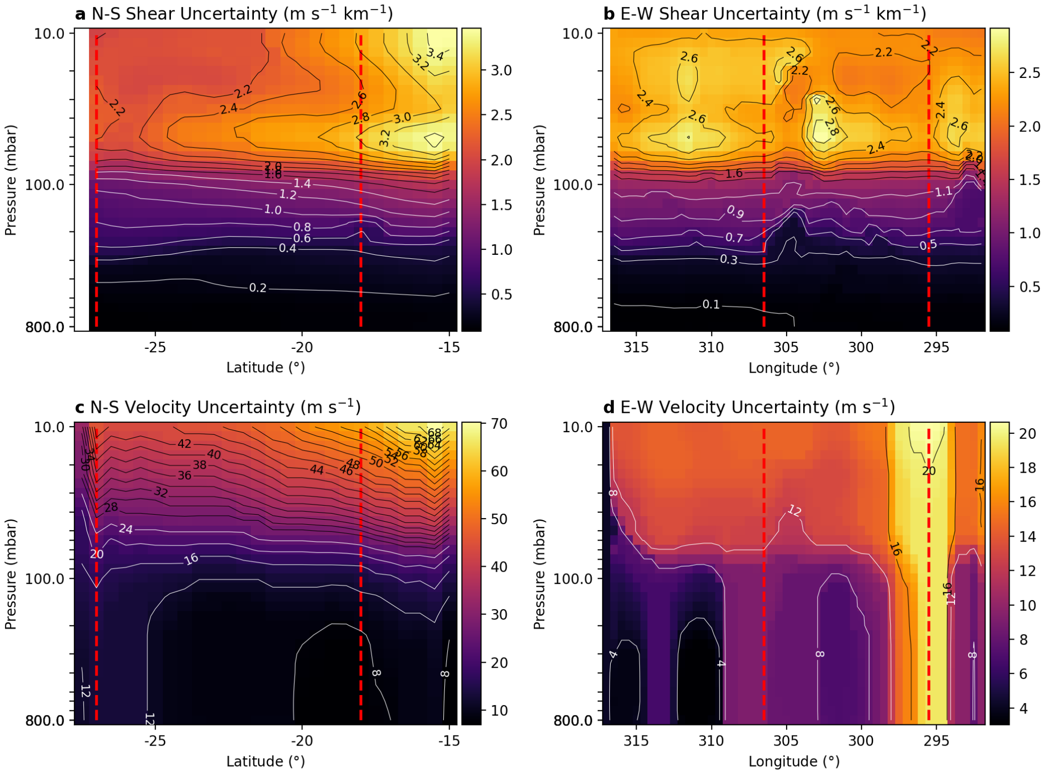

Figure S12: (a) and (b) Uncertainties in the derived August epoch thermal wind shear for the north-south and east-west directions respectively. Each plot passes through the centre of the GRS, located at (301.0°W, 22.5°S). Error propagation was used to determine these values using the uncertainties in both temperature and temperature gradient. (c) and (d) Uncertainties for the corresponding thermal wind velocities, derived by error propagation using the uncertainties of temperature, temperature gradient and prior wind velocity. An altitude of 1,200 mbar was assumed for the prior Hubble winds. For all plots, the boundaries of the GRS peak velocity field are denoted by the vertical dashed lines.

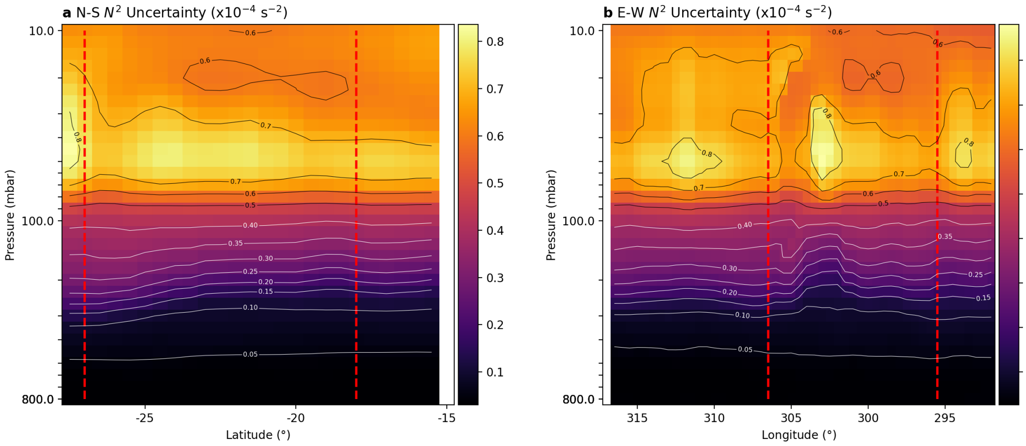

Figure S13: (a) Uncertainty in the derived August epoch north-south buoyancy frequency. (b) Uncertainty in the corresponding east-west buoyancy frequency. All uncertainties were determined by error propagation using the temperature and temperature gradient uncertainties. The boundaries of the GRS peak wind velocities in the Hubble prior data are denoted by the vertical red dashed lines. Each plot passes through the centre of the GRS, located at (301.0°W, 22.5°S).